FULL PAPER

Laminated Perovskite Layers

ADVANCED
FUNCTIONAL
MATERIALS

www.afm-journal.d

Solution-Processed Laminated Perovskite Layers for High-Performance Solar Cells

Yangyang Wang, Tianhao Li, Zengrong Li, Sen Wang, and Xianyu Deng*

Laminated multilayers of perovskite films with different optical and electronic characteristics will easily realize high-performance optoelectronic devices because it is widely demonstrated that differential distribution of film properties in the vertical direction of devices plays particularly important roles in device performance. However, the existing laminated perovskite films are hardly prepared by a solution process because there is no solvent with sufficient selectivity of solubility for different perovskite materials. Here, it is demonstrated that aniline (AN) has a largely different solubility toward the perovskite MAPbI$_3$ and the MAPbI$_3$ blend with an additive of hydrochloride diethylammonium chloride. By using AN as the solvent in the perovskite precursor solution, two laminated perovskite layers with different crystal size and optical and electrical characteristics are achieved. Inverted perovskite solar cells with the laminated films as active layers achieve an averaged power conversion efficiency of 20.65% originating from the high V_{OC} 1.112 V and fill factor of 80.8%. The devices maintain 98% efficiency after 400 h under 65% RH. This work provides a very simple and feasible method for production of laminated perovskite films to achieve high-performance perovskite solar cells.

1. Introduction

Perovskite solar cells have made significant progress, with the power conversion efficiency (PCE) rapidly enhanced from the original 3.8%[1] to ≈23% in the year of 2016 and 2017,[2–5] and lately over 24%.[6,7] Two typical methods, vacuum evaporation and solution process, were previously reported to prepare perovskite films for the solar cells. Compared with the former, the solution process has the advantages of easy deposition and is suitable for large-scale and flexible fabrication.[8–11] A common shortcoming is that it is difficult to form compact and uniform perovskite films using the solution process. To obtain high-quality perovskite films, some assistant methods have been employed in previous studies. These include adding select materials, such as organic amine hydrochloride,[12–14] polymers,[15,16] potassium iodide,[17] hydroiodic acid,[18] hydrochloric acid,[19] ethylammonium iodide (EAI),[20] and urea,[21]

as additives into perovskite precursor solutions and selecting various solvents such as dimethyl sulfoxide (DMSO),[2,3,22] γ-butyrolactone (GBL),[23] dimethylacetamide (DMA),[24] or acetonitrile (ACN)/ methylamine (MA)[25] to completely or partly replace the traditionally used solvent N,N-dimethylformamide (DMF).[1]

Another key challenge for the solution process to prepare the perovskite films is the difficulty of obtaining multilayered films because the first formed layer will be dissolved during the deposition of the second layer. This means that different perovskite films prepared by a solution process are difficultly used in a single device. This seriously limits the device performance because different perovskite films have their respective characteristics and advantages. For example, different materials usually have different bandgaps so that it will enlarge the absorption range by using them together, which is the main factor in achieving high efficiency by a multicomponent or laminated device structure in organic, perovskite, or hybrid solar cells.[5,26–28] Additionally, perovskite with a single component such as MAPbI$_3$ could have different structure and electronic characteristics due to different film-forming conditions and processes. Li and co-workers lately reported a perovskite homojunction structure incorporating a thermally evaporated p-type layer on top of a solution-processed n-type layer, which demonstrated a highly enhancement of device performance by the laminated perovskite film with different doping layers.[29] According to other literature, MAPbI$_3$ films with different sizes of crystals show different absorption and carrier transfer characteristics because of size effects and boundary confines.[30] It also has different abilities of holes and electrons transfer from the perovskite film to hole transfer layer (HTL) and electron transfer layer (ETL), respectively.[30–32] The transfer unbalance leads to carrier recombination, which reduces the efficiency of solar cells.[26] If two kinds of perovskites with different controlled crystal sizes can be combined, the transfer balance will be largely enhanced. Therefore, the combination of various perovskites in a single device can provide various important means to enhance the device performance.[33] However, because of the key challenge mentioned above, few multilayered perovskite films made by a solution process are reported for various perovskite-based optoelectronic devices.

Here, we demonstrated solution-processed multilayered perovskite films with different crystal sizes and electronic

Dr. Y. Wang, T. Li, Z. Li, S. Wang, Prof. X. Deng
Shenzhen Key Laboratory of Advanced Materials
School of Materials Science and Engineering
Harbin Institute of Technology
Shenzhen 518055, P. R. China
E-mail: xydeng@hit.edu.cn

1903330 (1 of 9)

properties by using aniline (AN) as a solvent. We note that AN has never been reported as a solvent for perovskite solutions. We found that $MAPbI_3$ was weakly soluble in AN, and it is a colloidal state of a turbid solution. The turbid solution state can be exactly controlled by tuning the concentration of $MAPbI_3$. By selecting a solution with proper $MAPbI_3$ concentration, perovskite films of microsize crystals can be prepared. However, after adding diethylammonium chloride (DEACl) into the solution, $MAPbI_3$ became completely soluble. Compact and uniform perovskite films of nanosize crystals can be rapidly formed by spin-coating the solution with DEACl as an additive. Because AN is a weak solvent for $MAPbI_3$, it is easy to overlay the perovskite film of microsize crystals onto the perovskite film of nanosize crystals. By our known, up to date, there are no multilayer perovskite films achieved by a solution process. Because of the different electric properties of the two films with different crystal sizes, inverted perovskite solar cells based on the two laminated layers have a high PCE near 21% and largely enhanced stability.

2. Results and Discussion

Perovskite $MAPbI_3$ has a hexahedral structure, as shown in **Figure 1**a, which consists of corner-sharing methylammonium cations ($CH_3NH_3^+$ or MA^+) connected with halide anions (I^-) standing at the face center, and a metal halide cation (Pb^{2+}) standing at the hexahedron center. The chemical structure of solvent AN and additive diethylammonium chloride (DEACl) is also shown in Figure 1a. The images in Figure S1 (Supporting Information) compare the solution states of different concentrations of $MAPbI_3$ in AN with or without the additive of DEACl. Figure S1 (Supporting Information) shows that $MAPbI_3$ originally is weakly soluble in AN with the state of colloid, and the dispersity of the solutions looks obviously different with the change of the concentration of $MAPbI_3$. However, with the addition of DEACl, all the solutions are clear, which means that $MAPbI_3$ has been completely solubilized. Here, we select two solutions, one is the $MAPbI_3$ (1 M) solution with DEACl (0.4 M) and the other is $MAPbI_3$ (1 M) colloid solution without DEACl, to form two laminated layers of perovskite films for fabricating solar cells. The right side of Figure 1a shows optical images of the two $MAPbI_3$ solutions. The film-forming process of the laminated layers is shown in Figure 1b. The total process can be divided into two steps: processes 1 and 2. In process 1, the thin film of nanocrystals was deposited by the spin-coating method, which was nearly same with our previously reported papers[14,34] with the exception of using AN to replace the DMF as the solvent. After an annealing process, the thin film of nanocrystals, with morphology shown in the left side of **Figure 2**a, was obtained. Then, in process 2, the other perovskite film of microcrystals was deposited on top of the film of nanocrystals, as shown in the bottom portion of Figure 1b. The method of vacuum-assistant blade-coating was employed in process 2. The $MAPbI_3$ colloid was dropped on the predeposited film, and then the glass rod was used to scrape the colloid to form a precursor film. After this, the film was put into a vacuum equipment to vaporize the solvent. The process of vacuum vapor is used to make the solvent vapor uniformly so that it can form a smooth film. The vacuum-treated film was then put on a hot plate and annealed for 10 min at 90 °C. Thus, a double-layered perovskite film with different size crystals was obtained. Here, the process of blade-coating, instead of the process of spin-coating, was used to prepare the upper layer of
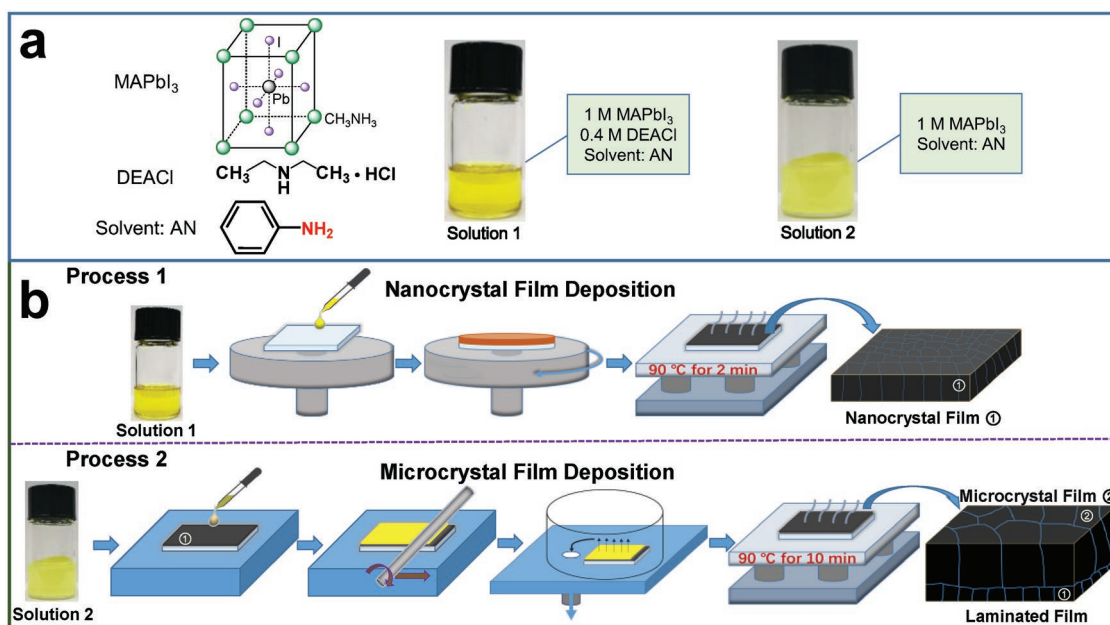

Figure 1. Main materials and preparation process of perovskite films. a) The chemical structures of main materials used in this study and the images of solutions with perovskite $MAPbI_3$ and DEACl dissolved in AN solvent. b) The schematic diagrams of the process to deposit $MAPbI_3$ films used in perovskite solar cell devices in this study. The upper and lower figures show the process to spin-coat nanocrystal film and to deposit nanomicrocrystal composite film using Solution 1 and Solution 2, respectively.
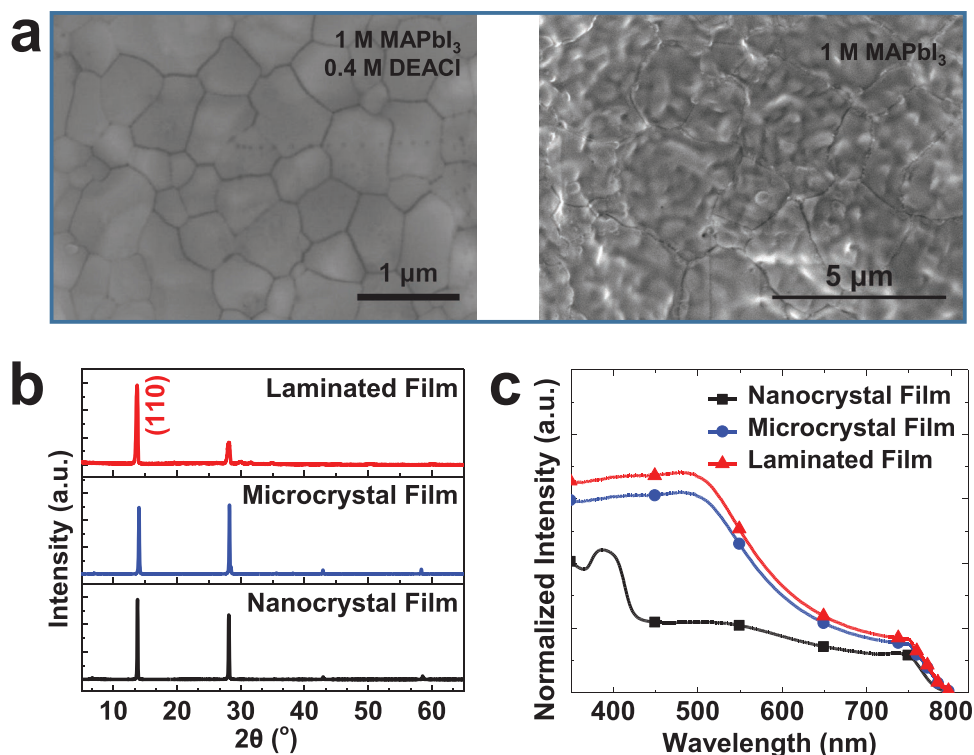
Figure 2. Characteristics of perovskite films. a) SEM images of the surface morphologies for perovskite MAPbI$_3$ films prepared via the process shown in Figure 1b (right: nanocrystal film; left: microcrystal film). b) The XRD and c) UV–vis absorption spectrum of the MAPbI$_3$ films, which all had a thickness of ≈450 nm. Nanocrystal film: film prepared via the process shown in upper of Figure 1b; microcrystal film: film deposited on glass via the process shown in lower of Figure 1b; laminated film: film deposited on nanocrystal film via the process shown in lower of Figure 1b.

perovskite. The reason is that the MAPbI$_3$ colloid solution can form a smooth and compact film by blade-coating but not by spin-coating.

To conveniently and simply express the different perovskite films, the film prepared from the solution 1 via the process 1, which was mainly composed of crystals with nanosizes, was defined as the "nanocrystal film." The film prepared from the solution 2 via the process 2, which was mainly composed of crystals with microsizes, was defined as the "microcrystal film." The film containing the microcrystal film on top of the nanocrystal film was defined as the "laminated film."

Scanning electron microscopy (SEM) measurements were performed to study the film morphology as shown in Figure 2. It is clear that with different solution states, the film morphology has distinct differences. The left of Figure 2a shows a compact, smooth, and uniform nanocrystal film with the crystal size range from 200 to 500 nm. The film is prepared from Solution 1 via Process 1. The right side of Figure 2a shows a microcrystal film prepared from Solution 2 via Process 2, which has crystals of size ≈5 µm. The crystal distributions of different perovskite films can also be seen from atomic force microscopy (AFM) shown in Figure S2 (Supporting Information). The larger crystals can lead to some characteristics, such as higher carrier migration velocity and wider absorption range. Figure 2b shows the X-ray diffraction (XRD) spectra of various perovskite films. All the films have the feature peaks of MAPbI$_3$ material, including two main peaks located at 14.08° and 28.20°, which correspond to the crystal faces of (110) and (220), respectively.

When the nanocrystal film was prepared, the intensity of (110) peak is stronger than the peak of (220). This means that this film has more crystallization orientation of (110). However, in the spectrum of microcrystal film, the intensity of (110) has no superiority compared with the peak of (220), indicating a decrease of crystallization. When the microcrystal film was deposited on top of the nanocrystal film, the double-layered film with high crystallization orientation was obtained, which implies that, in the double-layered film, the crystallization of the bottom nanocrystal film has large influence on the crystallization of the upper microcrystal perovskite film. Figure 2c shows the difference of light absorption for the three types of perovskite films. The size of crystal could have considerable effect on optical absorption of film due to the lower defect concentration[29] and crystal scattering.[35]

The solar cells were fabricated with the inverted structure shown in **Figure 3**a, in which the poly(3,4-ethylenedioxythiophene):polystyrene sulfonate (PEDOT:PSS) and [6,6]-phenyl-C$_{61}$-butyric acid methyl ester (PCBM) are used as HTL and ETL, respectively. Figure 3b is the section SEM image of the device. Although the coedge of the two layers is slightly bent, the edge line is clear enough to prove a double-layered structure. The thickness is ≈170 nm for the nanocrystal layer and 230 nm for the microcrystal layer. Their crystal sizes are ≈300 nm and over 1 µm, respectively. This perovskite film has compact and smooth surface morphology as shown in Figure S3 (Supporting Information). Compared with the single nanocrystal and microcrystal films shown in Figure S4
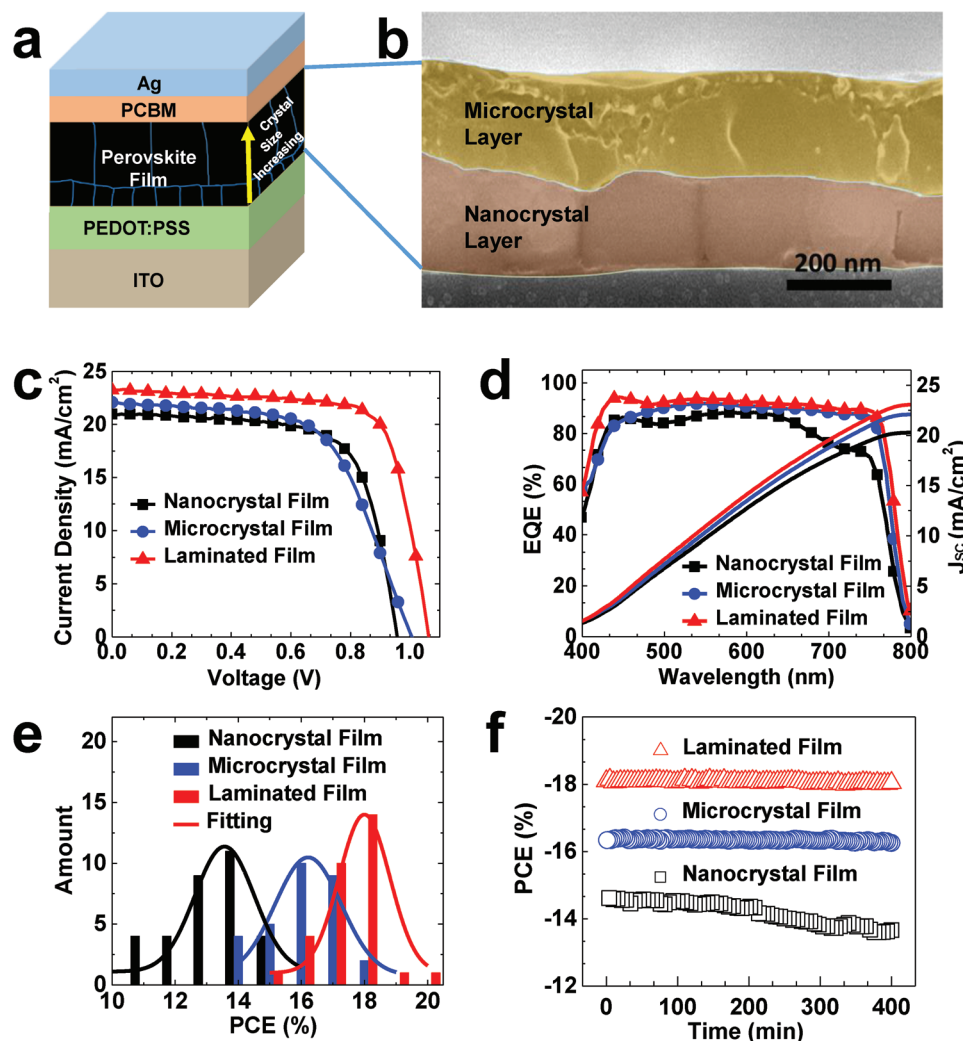
Figure 3. Device structure and performances. a) The device structure of the perovskite solar cell prepared in this study. b) The SEM images for section and morphology of heterojunction MAPbI$_3$ film deposited via the process shown in Figure 1b. The performances of perovskite solar cell devices based on different MAPbI$_3$ films. c) J–V (current density–voltage) and d) EQE curves of solar cells based on perovskite film with nanocrystals, microcrystals, and heterojunction crystals. e) The PCE distributions were summarized from the performances of 30 devices. f) The PCE changes of solar cells were recorded under AM1.5 illumination 100 mW cm^{-2} at room temperature without any encapsulation. The thickness of both the single nanocrystal and the single microcrystal films is about 450 nm, while the thickness of the nanocrystal and the microcrystal layers is about 200 and 250 nm, respectively, in the laminated film. The thickness of perovskite films were controlled by tuning the concentration of perovskite solution and processing parameters.

(Supporting Information), the composite film has some advantages. The spin-coated nanocrystal film is in tight contact with the substrate. However, there are obvious crevices between the scape-coated microcrystal film and the substrate. When the microcrystal film was deposited onto the nanocrystal film, the contact between double perovskite films is tight. Therefore, the double layer helps to achieve a highly improved contact between the layers in the device structure. Also, as shown in Figure S2 (Supporting Information), the AFM images indicate the average surface roughness (Ra) of nanocrystal, microcrystal, and laminated perovskite film were 24.7, 34, and 30.4 nm, respectively. The laminated film was smoother than the microcrystal film although they both have crystals with large size. This demonstrated that the growth of the crystal is strongly dependent on the substrate. A crystal substrate is also good for improving the surface smoothness of another crystal film grown on top of it.

Figure 3c–f and **Table 1** compare the device performances of three different solar cells, the devices based on the single layer of nanocrystal perovskite film (nanocrystal film), the single layer of microcrystal perovskite film (microcrystal film), and the double layer of laminated perovskite films (laminated films). From the results, the solar cell based on the laminated perovskite films exhibits the best performance, with all parameters largely enhanced. The nanocrystal film-based device has a PCE

Table 1. Performance of the solar cell based on various perovskite films.

Perovskite film	PCE [%]	J_{SC} [mA cm^{-2}]	V_{OC} [V]	FF [%]
Nanocrystal film	13.87	20.962	0.956	69.2
Microcrystal film	13.34	22.085	1.006	60.0
Laminated film	18.09	23.244	1.061	73.3

of 13.87%, along with the short-circuit current (J_{SC}), open-circuit voltage (V_{OC}), and fill factor (FF) of 20.962 mA cm^{-2}, 0.956 V, and 69.2%, respectively. When the perovskite film was replaced by scape-coating film with microcrystals, the PCE lowered a little to 13.34%. The large crystals in the microcrystal film lead to a high absorption efficient from the spectrum shown in Figure 2d, which results in the increase of J_{SC}. The external quantum efficiency (EQE) shown in Figure 3d also indicates that the large crystals lead to a higher light absorption in the wavelength range from 650 to 800 nm. However, because of the significant decline of FF, the PCE still decreased. The reason could mainly be the bad contact between PEDOT:PSS and perovskite film as shown in Figure S3b (Supporting Information). When laminating the nanocrystal and microcrystal perovskite films, both the light absorption and the interface contacts were improved, and a solar cell with a high PCE of 18.09% was achieved. The J_{SC}, V_{OC}, and FF were enhanced up to 23.244 mA cm^{-2}, 1.061 V, and 73.3%, respectively. The EQE curves (Figure 3d) proved the difference in light absorption, which corresponds to UV–vis spectrum shown in Figure 2c. J_{SC} calculated from the EQE spectrum have high consistency with that recorded from the J–V measurements. The effect of perovskite films on PCE distribution is exhibited in Figure 3e. These data indicate the device repeatability. When the laminated perovskite films are used, the range of the device PCE varies from 15 to 20%, and the fitting curve is sharper than that of the devices based on either the single nanocrystal film or the microcrystal film. In addition to the aforementioned performance, the laminated film-based device shows high stability. When the device PCEs were measured under simulated AM1.5 illumination of 100 mW cm^{-2} for 400 min, the change tendencies are shown in Figure 3f. There is only little change of PCE under long-time illumination for the device with the microcrystal film or the laminated films, while the PCE is obviously

reduced for the device with the nanocrystal film. The results from Figure 3f indicate that the microcrystal perovskite plays a key role on the device stability. The microcrystal perovskite with enlarged grain size has less grain boundary along the vertical direction of the film, which is beneficial for facilitating hole or electron transport.

To investigate the effect of crystallization orientation in perovskite films on the performance of solar cell devices, the grazing-incidence wide-angle X-ray scattering (GIWAXS) measurements were carried out. The scattering rings at $q = 1$ Å^{-1} in 2D GIWAXS patterns (**Figure 4**a–c) for the MAPbI$_3$ films are assigned to the (110) plane of the perovskite structures (Figure 2b). Clearly, the MAPbI$_3$ microcrystal film deposited on top of PEDOT:PSS via scape-coating method shows a uniform intensity distribution along the azimuthal angle at $q = 1$ Å^{-1} (Figure 4b), indicating little preference of the crystal orientation. The result proves that the microcrystal film has random crystal orientation of perovskites as shown in the upper portion of Figure 4d. However, for the MAPbI$_3$ nanocrystal film deposited on top of PEDOT:PSS via spin-coating method, the patterns exhibit scattering bright specks with intense scattering intensity at the azimuthal angle of 90°. This phenomenon means that the crystal planes in a nanocrystal film are highly oriented parallel to the substrate (lower of Figure 4d), which is beneficial for improving the charge transport property. These results are in accord with the XRD data shown in Figure 2b. Moreover, the MAPbI$_3$ microcrystal film was deposited on the MAPbI$_3$ nanocrystal film, as shown in Figure 2b. The crystal orientation of perovskite film is enhanced similarly to the nanocrystal film, which can be demonstrated by the increase of peak intensity for (110) (Figure 2b) and the scattering bright specks with intense scattering intensity at the azimuthal angle of 90° (Figure 4c). This interesting evolution comes from the crystal epitaxial growth, which is responsible for the orientated
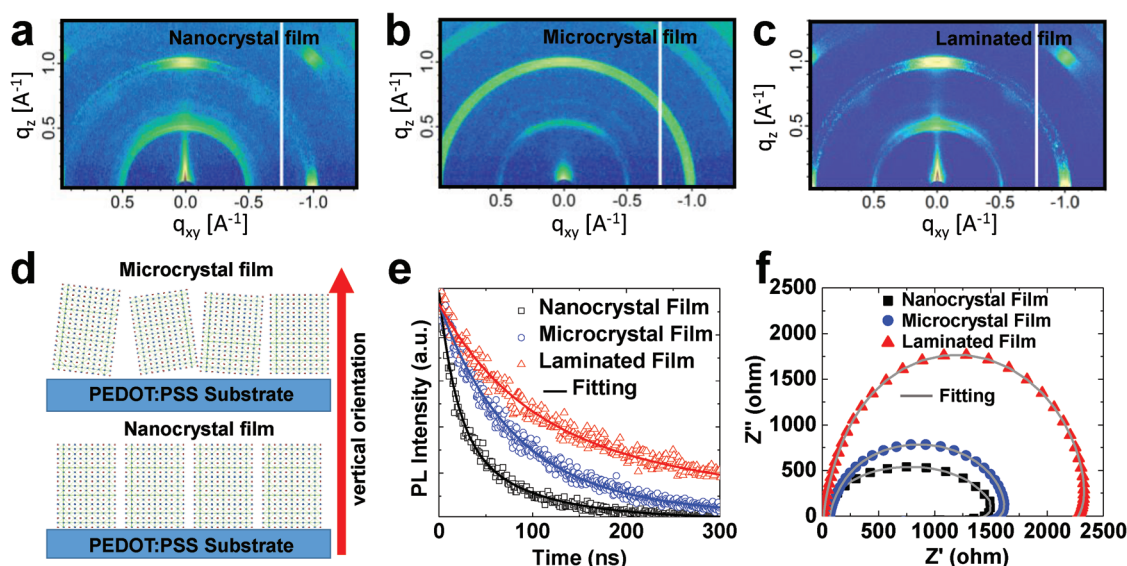

Figure 4. Discussion for effect of perovskite films on device performances. a–c) GIWAXS images of perovskite films deposited via various processes. d) Schematic illustration of crystal structural evolution in MAPbI$_3$ perovskite films. e) Normalized transient photoluminescence (PL) decay spectra (fitting data) for various perovskite films on glasses (excitation wavelength: 480 nm pulsed laser). f) Nyquist plots of the ITO/PEDOT:PSS/MAPbI$_3$/ PCBM/Ag devices with various MAPbI$_3$ layers.

**ADVANCED
SCIENCE NEWS**

www.advancedsciencenews.com

**ADVANCED
FUNCTIONAL
MATERIALS**

www.afm-journal.de

growth of the film dependent on the substrate crystallization. The higher crystal orientation of the MAPbI$_3$ film will be helpful for the charge transfer so that the device performance will be enhanced.[36]

Transient photoluminescence (PL) and electrochemical impedance spectroscopy (EIS) measurements were carried out to further compare the optical and electrical properties of the different films. The results of the PL are shown in Figure 4d. Fitting the transient PL can simulate two decay times of τ_1 and τ_2 that represent the nonradiative recombination at the defect sites and the radiative recombination in perovskite films, respectively.[25,37,38] The data are summarized in Table S1 (Supporting Information). From the data, there are obvious changes for charge combinations in perovskite films due to the evolution of crystal structure and crystal size. The double-layered film shows a long lifetime of 228.9 ns, while the single nanocrystal film and the single microcrystal film have lifetimes of 66.2 and 147.1 ns, respectively. This result demonstrates that the laminated film has fewer defects and better charge transfer properties due to its high crystal orientation and large crystal size. The EIS data are shown in Figure 4e. The equivalent circuit used to fit the tested curves is shown in Figure S5a (Supporting Information), where R_s represents the contact resistance among different layers and the recombination resistance (R_{rec}) represents the charge transfer in the perovskite, which is ascribed to the low-frequency element in EIS.[39] The value of R_{rec} is associated with the charge recombination. The fitting values of R_s and R_{rec} are shown in Table S2 (Supporting Information). As shown in Figure S5b and Table S2 (Supporting Information), the values of R_s are 29.6 and 11.2 Ω for single nanocrystal film and the laminated film on top of PEDOT:PSS, respectively. However, the R_s value is large, that is, 65.3 Ω for the single microcrystal film on top of PEDOT:PSS, because of the poor contact between PEDOT:PSS and perovskite film. This result is consistent with the FF of solar cells from the exhibition of J–V curves in Figure 3c. Additionally, the large increase of R_{rec} for the device with the laminated perovskite films implies that the combination of nanocrystal film and microcrystal film results in lowering the charge recombination in the perovskite films. These results are also in accordance with the PL data shown in Figure 4d. Therefore, it has been demonstrated that the laminated film has low defects for high charge transfer efficiency.

Another important advantage of the laminated two perovskite films in a device is that it can enhance the balance of charge transport. Electrons and holes find it difficult to keep a balance in the device only with a single perovskite layer owing to the mobility difference of the carriers. Two layers will easily overcome the problem. To investigate the transport properties of the films, hole- or electron-only devices were fabricated. The J–V curves of the devices are given in Figure S6 (Supporting Information). By the mode of space charge limited current (SCLC), the trap density and carrier mobility can be calculated and have results as listed in Table S3 (Supporting Information). According to the results, the ratio of hole mobility to electron mobility (μ_h/μ_e) is 1.76 for the nanocrystal-based device and 2.10 for the microcrystal-based device, while it is only 1.06 for the laminated films-based device. As well as the balance of the carrier mobility, the laminated films-based device shows a

much larger mobility of both holes and electrons as compared to the other two devices. The trap density of the laminated films is also lower than that of the other two films, which is consistent with the results of the transient PL and EIS in the above discussion.

To further enhance the performances of the solar cells, the interfacial modification was introduced for the interfaces at two electrodes. Graphene oxide (GO) and MoS$_2$ were inserted at the interfaces of anode and cathode, respectively. The deposition of the interfacial layers is the same as the method described in our previous report.[34] The device structure with the interfacial modifications is shown in **Figure 5**a. To compare with the new device based on the laminated perovskite films, the device based on MAPbI$_3$ film was prepared via the traditional spin-coating method in which MAPbI$_3$ is dissolved in DMF with DEACl as an additive.[14,34] Figure 5b shows the J–V curves of the two devices. The newly designed device based on the laminated perovskite films shows PCE up to 20.65% along with the J_{SC}, V_{OC}, and FF of 22.983 mA cm^{-2}, 1.112 V, and 80.8%, respectively (Table S4, Supporting Information). Not only the device performance but also the manufacture repeatability is enhanced (Figure 5c). The PCE of the new device ranges from 18 to 21%, which is further concentrated by comparing with that of the control device varying from 16 to 20%. This means that it is more suitable for quantity production. The newly designed device also has better device stability, which is attributed to the laminated MAPbI$_3$ films with better charge transfer and large crystals on the surface. Figure 5d shows that the newly designed device kept the high stability of within 400 h at 25 °C under 65% relative humidity (RH). The large crystals lead to fewer crystal boundaries. The crystal boundaries in perovskite films are considered a main factor causing the aggregation of I$^-$ ions and the decomposition of perovskite.[40–42] Therefore, it has high stability, and the device maintains 98% efficiency after 400 h under 65% RH. Although the PCE and the stability were enhanced to a higher level by the modification of the interfaces at electrodes, the laminated films in this work inevitably have a distinct interface between the two perovskite films. An interfacial recombination may exist near the boundary for the laminated films. Therefore, the device performance could be further modified in future by the research of the interface between the two films.

3. Conclusion

In summary, laminated layers of perovskite films were realized by using aniline as a solvent of the perovskite precursor solutions. MAPbI$_3$ was weakly soluble in AN with the colloidal state of a turbid solution, while after adding some DEACl into the solutions, MAPbI$_3$ became completely soluble. By spin-coating the two solutions in order on top of the substrate of PEDOT:PSS-covered ITO, two laminated perovskite layers with different crystal size, one for nanocrystal size and the other for microcrystal size, were prepared. The two films showed different electric properties and both had high crystal orientation so that the laminated films had high carrier mobility. Due to these characteristics, inverted perovskite solar cells based on two laminated layers showed a high performance of averaged
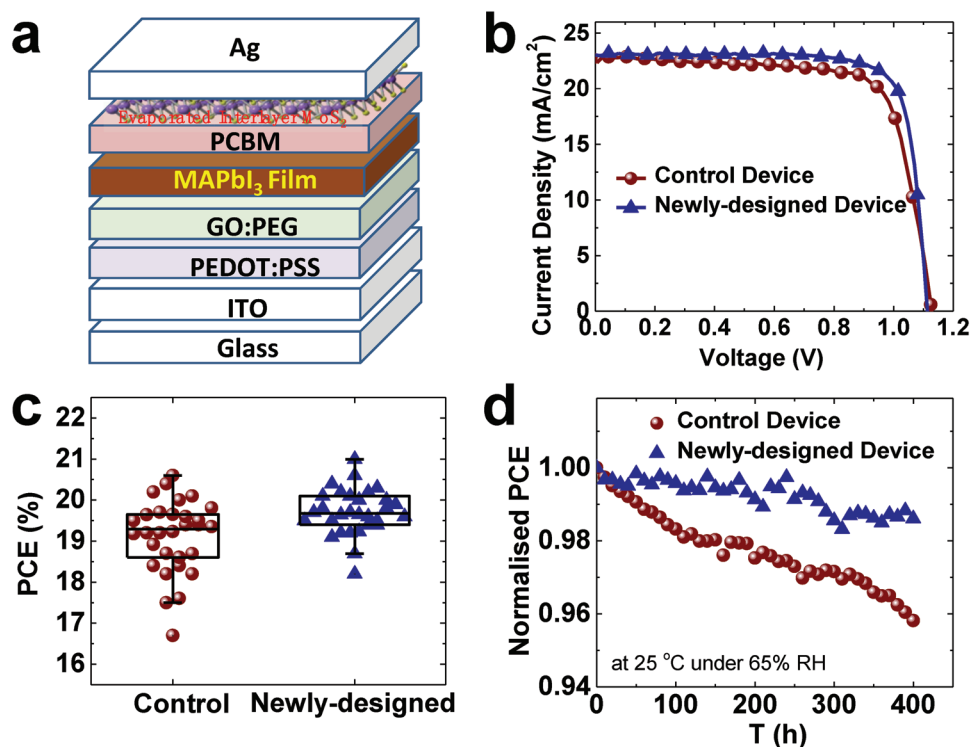
ADVANCED
SCIENCE NEWS
www.advancedsciencenews.com

ADVANCED
FUNCTIONAL
MATERIALS
www.afm-journal.de

Figure 5. Device performances of solar cells with interface modification layers. Device performance of solar cells based on the traditional single-layer perovskite film (control device) and the newly designed laminated perovskite films (newly designed device) after interfacial modifications with GO and MoS$_2$. a) The schematic diagram of device structure for solar cell device based on MAPbI$_3$ films modified with GO and MoS$_2$ interface layers. b) J–V curves of the solar cells devices. c) Statistics of the PCE distribution for the corresponding devices which are summarized from the data of 30 samples for every kind of device. d) Humidity stability of the corresponding devices at 25 °C under 65% relative humidity (RH) without any encapsulation. In control device: The MAPbI$_3$ films were prepared by spin-coating the precursor solution of MAPbI$_3$ and DEACl dissolved in DMF. Newly designed device: The MAPbI$_3$ films were laminated films deposited via the corresponding process in this work.

PCE 20.65% as well as largely enhanced stability. This work provides a very simple and feasible way for the manufacture of laminated perovskite films to meet the requirements for the differential distribution of film properties in perovskite devices to achieve high-performance solar cells.

4. Experimental Section

Materials: Indium tin oxide (ITO) with a sheet resistance of 7 Ω sq^{-1} was purchased from CSG Holding Co., Ltd. PEDOT:PSS (4083), PbI$_2$ (99.998%), and MAI (CH$_3$NH$_3$$^+$=MA$^+$, 99.99%) were bought from Xi'an Polymer Light Technology Corp. (PLT). DMF (anhydrous), AN (99.5%, anhydrous), and DEACl were purchased from Sigma-Aldrich.

Preparation and Characterization of Perovskite Films: To deposit the MAPbI$_3$ films, perovskite solutions were first prepared. For AN solution of MAPbI$_3$, PbI$_2$ and MAI were dissolved in AN at a molar ratio of 1:1 and the concentration of PbI$_2$ was 0.05, 0.1, 0.6, or 1.0 M. All solutions were stirred for 24 h at room temperature. The MAPbI$_3$ and DEACl mixture solutions were prepared by dissolving MAI, PbI$_2$, and DEACl in DMF or AN with a mole ratio of 1:1:0.4 and stirring for 24 h on a hot plate at 70 °C, respectively. Then, the solutions were spin-coated on washed glasses at a speed of 4000 rpm for 30 min, and the films were annealed for 10 min at 90 °C. All the films were measured using field emission scanning electron microscopy (FESEM, HITACHI S-4700), XRD (D/Max 2500PC), AFM (CSPM5500), and UV–vis absorption spectra (U-3010Hitachi). GIWAXS was done via a detector with a wavelength of 1.34 nm.

Fabrication and Characterization of Perovskite Solar Cells: For the fabrication of the devices, first, ITO substrates with patterns were

ultrasonically cleaned by detergent, deionized water, acetone, and isopropyl alcohol for 10 min each. Then, PEDOT:PSS (4083) was spin-coated on the cleaned ITO with a speed of 3500 rpm for 30 s, and annealed on a hot plate at 130 °C for 1 h in N$_2$ glove box. The GO (10 mg mL^{-1}):PEG (1 mg mL^{-1}) blend solution was spin-coated on PEDOT:PSS films at the rate of 3000 rpm for 30 s and annealed on a hot plate at 90 °C for 30 min. After the modifier films were prepared, the MAPbI$_3$ films were deposited. For the nanocrystal films, the MAPbI$_3$ and DEACl mixture solutions were spin-coated at a speed of 4000 rpm for 30 s. After spin-coating, the sample was annealed on a hot plate at 90 °C for 10 min. Then, the microcrystal films were manufactured via scape-coating method with an AN solution of MAPbI$_3$ and annealed for 10 min at 90 °C. After the perovskite film was formed, a PCBM solution, 15 mg PCBM added into 1 mL of chlorobenzene, was spin-coated on top of the perovskite film at a speed of 1500 rpm for 30 s. Finally, 3 nm MoS$_2$ and 120 nm silver (Ag) films were deposited on top of the PCBM layer via a thermal-evaporation process in a vacuum chamber with a pressure of less than 10^{-4} Pa. The typical active area of the devices was ≈0.12 cm^2, which was determined by a shadow mask during the top electrode evaporation. The current density (J)–voltage (V) was recorded using a Keithley 2400 source meter unit where the solar light source was simulated by AM 1.5 sunlight with an intensity of 100 mW cm^{-2} provided by a solar simulator. J–V measurements were carried out in the N$_2$ glove box. The EQE measurements were carried out with a quantum efficiency (QE)/monochromatic incident photon-to-electron conversion efficiency measurement system (SR830, Stanford Research Systems). A standard Si photodiode calibrated from Hamamatsu was tested as a reference prior to each sample measurement. EQE was measured in air on the condition of the devices with encapsulation. Steady-state measurements of the solar cell devices were carried out with an electrochemical workstation

(CS150H, Wuhan Corrtest Instruments Corp., Ltd.). Time-resolved transient PL spectra were obtained using a PL spectrometer, FLS 900, Edinburgh Instruments; excited with a picosecond pulsed diode laser (EPL-445); and measured at 405 nm after excitation. EIS measurements were conducted using a frequency response analyzer (PSM1735 NumetriQ) from 1 to 10^6 Hz under dark condition at a 1 V applied bias.

Supporting Information

Supporting Information is available from the Wiley Online Library or from the author.

Acknowledgements

Conflict of Interest

The authors declare no conflict of interest.

Keywords

[1] A. Kojima, K. Teshima, Y. Shirai, T. Miyasaka, *J. Am. Chem. Soc.* **2009**, *131*, 6050.
[2] W. S. Yang, B.-W. Park, E. Jung, N. J. Jeon, Y. C. Kim, D. U. Lee, S. S. Shin, J. Seo, E. Kim, J. H. Noh, S. I. Seok, *Science* **2017**, *356*, 1376.
[3] Q. Jiang, Z. Chu, P. Wang, X. Yang, H. Liu, Y. Wang, Z. Yin, J. Wu, X. Zhang, J. You, *Adv. Mater.* **2017**, *29*, 1703852.
[4] M. Saliba, T. Matsui, J.-Y. Seo, K. Domanski, J.-P. Correa-Baena, M. K. Nazeeruddin, S. M. Zakeeruddin, W. Tress, A. Abate, A. Hagfeldt, M. Grätzel, *Energy Environ. Sci.* **2016**, *9*, 1989.
[5] K. A. Bush, A. F. Palmstrom, Z. J. Yu, M. Boccard, R. Cheacharoen, J. P. Mailoa, D. P. McMeekin, R. L. Z. Hoye, C. D. Bailie, T. Leijtens, I. M. Peters, M. C. Minichetti, N. Rolston, R. Prasanna, S. Sofia, D. Harwood, W. Ma, F. Moghadam, H. J. Snaith, T. Buonassisi, Z. C. Holman, S. F. Bent, M. D. McGehee, *Nat. Energy* **2017**, *2*, 17009.
[6] M. Kim, G.-H. Kim, T. K. Lee, I. W. Choi, H. W. Choi, Y. Jo, Y. J. Yoon, J. W. Kim, J. Lee, D. Huh, H. Lee, S. K. Kwak, J. Y. Kim, D. S. Kim, *Joule* **2019**, https://doi.org/10.1016/j.joule.2019.06.014.
[7] https://www.nrel.gov/pv/cell-efficiency.html (accessed: August 2019).
[8] H.-C. Liao, P. Guo, C.-P. Hsu, M. Lin, B. Wang, L. Zeng, W. Huang, C. M. M. Soe, W.-F. Su, M. J. Bedzyk, M. R. Wasielewski, A. Facchetti, R. P. H. Chang, M. G. Kanatzidis, T. J. Marks, *Adv. Energy Mater.* **2017**, *7*, 1601660.
[9] A. Priyadarshi, L. J. Haur, P. Murray, D. Fu, S. Kulkarni, G. Xing, T. C. Sum, N. Mathews, S. G. Mhaisalkar, *Energy Environ. Sci.* **2016**, *9*, 3687.
[10] E. Bi, H. Chen, F. Xie, Y. Wu, W. Chen, Y. Su, A. Islam, M. Grätzel, X. Yang, L. Han, *Nat. Conmun.* **2017**, *8*, 15330.
[11] J. Feng, X. Zhu, Z. Yang, X. Zhang, J. Niu, Z. Wang, S. Zuo, S. Priya, S. (F.) Liu, D. Yang, *Adv. Mater.* **2018**, *30*, 1801418.
[12] L. Zhao, D. Luo, J. Wu, Q. Hu, W. Zhang, K. Chen, T. Liu, Y. Liu, Y. Zhang, F. Liu, T. P. Russell, H. J. Snaith, R. Zhu, Q. Gong, *Adv. Funct. Mater.* **2016**, *26*, 3508.
[13] Y. Zhao, K. Zhu, *J. Phys. Chem. C* **2014**, *118*, 9412.
[14] Y. Wang, N. Song, L. Feng, X. Deng, *ACS Appl. Mater. Interfaces* **2016**, *8*, 24703.
[15] Y. Wang, J. Luo, R. Nie, X. Deng, *Energy Technol.* **2016**, *4*, 473.
[16] D. Bi, C. Yi, J. Luo, J.-D. Décoppet, F. Zhang, S. M. Zakeeruddin, X. Li, *Nat. Energy* **2016**, *1*, 16142.
[17] M. Abdi-Jalebi, Z. Andaji-Garmaroudi, S. Cacovich, C. Stavrakas, B. Philippe, J. M. Richter, M. Alsari, E. P. Booker, E. M. Hutter, A. J. Pearson, S. Lilliu, T. J. Savenije, H. Rensmo, G. Divitini, C. Ducati, R. H. Friend, S. D. Stranks, *Nature* **2018**, *555*, 497.
[18] F. Wang, H. Yu, H. Xu, N. Zhao, *Adv. Funct. Mater.* **2015**, *25*, 1120.
[19] G. Li, T. Zhang, Y. Zhao, *J. Mater. Chem. A* **2015**, *3*, 19674.
[20] H.-L. Hsu, C.-C. Chang, C.-P. Chen, B.-H. Jiang, R.-J. Jeng, C.-H. Cheng, *J. Mater. Chem. A* **2015**, *3*, 9271.
[21] J.-W. Lee, S.-H. Bae, Y.-T. Hsieh, N. D. Marco, M. Wang, P. Sun, Y. Yang, *Chem* **2017**, *3*, 290.
[22] N. Ahn, D.-Y. Son, I.-H. Jang, S. M. Kang, M. Choiand, N.-G. Park, *J. Am. Chem. Soc.* **2015**, *137*, 8696.
[23] H.-B. Kim, H. Choi, J. Jeong, S. Kim, B. Walker, S. Song, J. Y. Kim, *Nanoscale* **2014**, *6*, 6679.
[24] M. Lv, X. Dong, X. Fang, B. Lin, S. Zhang, X. Xu, J. Ding, N. Yuan, *RSC Adv.* **2015**, *5*, 93957.
[25] N. K. Noel, S. N. Habisreutinger, B. Wenger, M. T. Klug, M. T. Hörantner, M. B. Johnston, R. J. Nicholas, D. T. Moore, H. J. Snaith, *Energy Environ. Sci.* **2017**, *10*, 145.
[26] J. Zhang, D. Bai, Z. Jin, H. Bian, K. Wang, J. Sun, Q. Wang, S. (F.) Liu, *Adv. Energy Mater.* **2018**, *8*, 1703246.
[27] B. Chen, Y. Bai, Z. Yu, T. Li, X. Zheng, Q. Dong, L. Shen, M. Boccard, A. Gruverman, Z. Holman, J. Huang, *Adv. Energy Mater.* **2016**, *6*, 1601128.
[28] F. Sahli, J. Werner, B. A. Kamino, M. Bräuninger, R. Monnard, B. Paviet-Salomon, L. Barraud, L. Ding, J. J. D. Leon, D. Sacchetto, G. Cattaneo, M. Despeisse, M. Boccard, S. Nicolay, Q. Jeangros, B. Niesen, C. Ballif, *Nat. Mater.* **2018**, *17*, 820.
[29] P. Cui, D. Wei, J. Ji, H. Huang, E. Jia, S. Dou, T. Wang, W. Wang, M. Li, *Nat. Energy* **2019**, *4*, 150.
[30] Q. Dong, Y. Fang, Y. Shao, P. Mulligan, J. Qiu, L. Cao, J. Huang, *Science* **2015**, *347*, 967.
[31] G. Xing, N. Mathews, S. Sun, S. S. Lim, Y. M. Lam, M. Grätzel, S. Mhaisalkar, T. C. Sum, *Science* **2013**, *342*, 344.
[32] D. Luo, W. Yang, Z. Wang, A. Sadhanala, Q. Hu, R. Su, R. Shivanna, G. F. Trindade, J. F. Watts, Z. Xu, T. Liu, K. Chen, F. Ye, P. Wu, L. Zhao, J. Wu, Y. Tu, Y. Zhang, X. Yang, W. Zhang, R. H. Friend, Q. Gong, H. J. Snaith, R. Zhu, *Science* **2018**, *360*, 1442.
[33] K. Lin, J. Xing, L. N. Quan, F. P. G. Arquer, X. Gong, J. Lu, L. Xie, W. Zhao, D. Zhang, C. Yan, W. Li, X. Liu, Y. Lu, J. Kirman, E. H. Sargent, Q. Xiong, Z. Wei, *Nature* **2018**, *562*, 245.
[34] Y. Wang, S. Wang, X. Chen, Z. Li, J. Wang, T. Li, X. Deng, *J. Mater. Chem. A* **2018**, *6*, 4860.
[35] J. Xue, Y. Gu, Q. Shan, Y. Zou, J. Song, L. Xu, Y. Dong, J. Li, H. Zeng, *Angew. Chem., Int. Ed.* **2017**, *56*, 5232.
[36] M. Jung, T. J. Shin, J. Seo, G. Kim, S. I. Seok, *Energy Environ. Sci.* **2018**, *11*, 2188.
[37] D. Shi, V. Adinolfi, R. Comin, M. Yuan, E. Alarousu, A. Buin, Y. Chen, S. Hoogland, A. Rothenberger, K. Katsiev, Y. Losovyj, X. Zhang, P. A. Dowben, O. F. Mohammed, E. H. Sargent, O. M. Bakr, *Science* **2015**, *347*, 519.

[38] A. A. Zhumekenov, M. I. Saidaminov, M. Haque, E. Alarousu, S. P. Sarmah, B. Murali, I. Dursun, X.-H. Miao, A. L. Abdelhady, T. Wu, O. F. Mohammed, O. M. Bakr, *ACS Energy Lett.* **2016**, *1*, 32.

[39] F. Wang, W. Geng, Y. Zhou, H.-H. Fang, C.-J. Tong, M. A. Loi, L.-M. Liu, N. Zhao, *Adv. Mater.* **2016**, *28*, 9986.

[40] J. S. Yun, J. Seidel, J. Kim, A. M. Soufiani, S. Huang, J. Lau, N. J. Jeon, S. Il Seok, M. A. Green, A. Ho-Baillie, *Adv. Energy Mater.* **2016**, *6*, 1600330.

[41] J. Li, Q. Dong, N. Li, L. Wang, *Adv. Energy Mater.* **2017**, *7*, 1602922.

[42] A. Guerrero, J. You, C. Aranda, Y. S. Kang, G. Garcia-Belmonte, H. Zhou, J. Bisquert, Y. Yang, *ACS Nano* **2016**, *10*, 218.